Monthly Notices
of the
ROYAL ASTRONOMICAL SOCIETY

MNRAS **468,** 3499–3515 (2017)
Advance Access publication 2017 February 23

doi:10.1093/mnras/stx440

# Identification of partially resolved binaries in Pan-STARRS 1 data

N. R. Deacon,[1,2]★ E. A. Magnier,[3] William M. J. Best,[3] Michael C. Liu,[3] T. J. Dupuy,[4] K. C. Chambers,[3] P. W. Draper,[5] H. Flewelling,[3] N. Metcalfe,[5] J. L. Tonry,[3] R. J. Wainscoat[3] and C. Waters[3]

[1]*Centre for Astrophysics Research, University of Hertfordshire, College Lane, Hatfield AL10 9AB, UK*
[2]*Max Planck Institute for Astronomy, Konigstuhl 17, D-69117 Heidelberg, Germany*
[3]*Institute for Astronomy, University of Hawaii at Manoa, 2680 Woodlawn Drive, Honolulu, HI 96822, USA*
[4]*Department of Astronomy, The University of Texas at Austin, 2515 Speedway, Austin, TX 78712, USA*
[5]*Department of Physics, University of Durham, South Road, Durham DH1 3LE, UK*

Accepted 2017 February 17. Received 2017 February 15; in original form 2016 October 23

**ABSTRACT**

Using shape measurement techniques developed for weak lensing surveys, we have identified three new ultracool binaries in the Pan-STARRS 1 (Chambers et al.) survey. Binary companions that are not completely resolved can still alter the shapes of stellar images. These shape distortions can be measured if point spread function anisotropy caused by the telescope is properly accounted for. We show using both a sample of known binary stars and simulated binaries that we can reliably recover binaries wider than around 0.3 arcsec and with flux ratios greater than around 0.1. We then applied our method to a sample of ultracool dwarfs within 30 pc with 293 objects having sufficient Pan-STARRS 1 data for our method. In total, we recovered all but one of the 11 binaries wider than 0.3 arcsec in this sample. Our one failure was a true binary detected with a significant but erroneously high ellipticity that led it to be rejected in our analysis. We identify three new binaries, one a simultaneous discovery, with primary spectral types M6.5, L1 and T0.5. These latter two were confirmed with Keck/Near Infrared Camera 2 follow-up imaging. This technique will be useful for identifying large numbers of stellar and substellar binaries in the upcoming Large Synoptic Survey Telescope and Dark Energy Survey sky surveys.

**Key words:** binaries: visual – brown dwarfs.

## 1 INTRODUCTION

Double stars, both coincident alignments and true physical systems, are common in the sky. These objects often present opportunities e.g. with binary systems serving as excellent benchmarks to characterize substellar evolutionary models (Liu, Dupuy & Ireland 2008). Binary stars have a common age and thus can be used to test the accuracy of stellar and substellar evolution models. The statistical properties of large samples of binary stars also represent a key output metric for star formation models. There are also problems introduced by binarity, such as the effect that hidden secondary components have on determinations of the initial mass function (see Chabrier 2003 for an example of how significant this can be). Transit surveys for exoplanets can be contaminated by stellar blends (Sirko & Paczynski 2003), as a background eclipsing binary blended with the target star can induce an erroneous planetary transit detection. Similarly, the radius of a real planet orbiting one component of an unidentified stellar binary may be significantly underestimated. Hence, large campaigns of both seeing-limited and adaptive-optics observations have been undertaken to weed out stellar blends from samples of candidate exoplanet host stars (see, for example, Law et al. 2014).

A novel method for detecting stellar binaries proposed by Hoekstra, Wu & Udalski (2005) uses image shape analysis developed for weak lensing detections in extragalactic astrophysics (Kaiser, Squires & Broadhurst 1994; Hoekstra et al. 1998) to identify stars with pronounced ellipticity, implying two sources blended together. Terziev et al. (2013) expanded this method to wide-field multi-epoch surveys, specifically the Palomar Transient Factory (PTF; Law et al. 2009). They demonstrated that both ellipticity and the trend of increasing ellipticity with better seeing could identify candidate double stars. These were confirmed using Robo-AO (Baranec et al. 2012) follow-up observations, demonstrating that the vast majority of stellar images identified as elliptical in their test sample were stellar blends and that the majority of stellar images with negligible ellipticity had no resolvable companion.

In this paper, we present an initial application of this method to Pan-STARRS 1 (PS1) data, showing that the stellar binaries identified by Terziev et al. (2013) can be readily identified using

★ E-mail: n.deacon2@herts.ac.uk

PS1. We then apply this technique to a sample of bright, nearby L and T dwarfs and identify three new binaries, one each of spectral types M, L and T. Finally, we discuss how this technique can be used with the PS1 data base as a whole, allowing users to identify partially resolved binaries for any sample of input objects. This method will allow large samples of stars to be screened for binarity in the 0.3–1.5 arcsec separation range, enabling cleaner samples for exoplanet transit studies such as *Kepler K2* (Howell et al. 2014). This is a larger lower resolution bound than space-based telescopes such as *Gaia* (20 mas, http://sci.esa.int/gaia/31441-binary-stars/) and the ∼15 mas possible from advanced aperture masking techniques used in ground-based observations (Kraus & Ireland 2012). The planned Large Synoptic Survey Telescope (LSST) will provide sharper, more frequent sampling of the sky, allowing this technique to be pushed to even smaller separations.

In Section 2, we use the test sample from Terziev et al. (2013) and simulated images to test to potential of this technique with PS1 data. In Section 3, we use this technique to identify new binaries in a sample of nearby ultracool dwarfs. In Section 4, we examine how this technique can be incorporated into the PS1 data base.

## 2 SHAPE MEASUREMENT

Shape measurement of astronomical objects has long been used to determine object morphology and multiplicity. The recent boom in cosmological parameter estimation based on weak gravitational lensing is built on the shape measurement formalisms developed by Kaiser et al. (1994) and Hoekstra et al. (1998). These imagine an idealized astronomical image above the atmosphere being distorted by both the atmosphere and telescope and decompose this distortion into two components, shear and smear. Shear is the stretching of an image by gravitational lensing or telescope, while smear is the fattening of the image caused by either seeing in the atmosphere or by the telescope optics. While we expect no significant gravitational shear on stars in the solar neighbourhood, the anisotropy introduced by the telescope optics will lead to point-like objects having significant ellipticities. Hoekstra et al. (2005) demonstrated that the weak lensing formalism can be used to correct for the shearing effect of the atmosphere and telescope to measure corrected ellipticities of stellar images.

Ellipticities are dimensionless numbers produced by combinations of the second position moments of the flux. These moments are defined thus,

$$I_{11} = \sum f(x,y)x^2W(x,y) \quad I_{12} = \sum f(x,y)xyW(x,y) \quad I_{22} = \sum f(x,y)y^2W(x,y). \quad (1)$$

Here $x$ and $y$ are pixel positions with respect to the star's photocentre, $f(x,y)$ is the flux in a particular pixel and $W(x,y)$ is a weighting function. This latter term suppresses values further from the photocentre to prevent noisy, low signal-to-noise (S/N) data dominating the moments. These moments are combined to form two dimensionless ellipticity parameters,

$$e_1 = \frac{I_{11} - I_{22}}{I_{11} + I_{22}} \quad e_2 = \frac{I_{12}}{I_{11} + I_{22}}. \quad (2)$$

The $e_1$ ellipticity polarization represents elongations along the R.A. and Declination axes, that is, the '+' polarization; while the $e_2$ ellipticity polarization represents elongations on axes tilted by 45°, the '×' polarization. These ellipticity values can be positive or negative with more elliptical stars having higher total ellipticities ($e_{\rm tot}$, the quadrature sum of $e_1$ and $e_2$). The individual ellipticity parameters are themselves a function of total ellipticity and the position angle of the binary. If we consider a binary with position angle $\theta$ measured as $\theta = \tan^{-1}\frac{x}{y}$, then the individual ellipticity values will take the following form

$$e_1 = -e_{\rm tot}\cos 2\theta \qquad e_2 = e_{\rm tot}\sin 2\theta. \quad (3)$$

The values of $e_1$ and $e_2$ are symmetric with a 180° rotation. See Terziev et al. (2013)'s section 5.2 for a similar derivation of the relationship between ellipticity values and position angle. Note that in later sections, we will see a subtly different version of this formula as the result of mapping R.A. to PS1 image pixel number. The remainder of this section briefly describes the corrections made to the values of $e_1$ and $e_2$ by Hoekstra et al. (2005). Any reader interested in the technical details of this method should refer to that paper. Note that below we use the suffix $\nu$ to refer to both the ellipticity polarizations. Thus, $e_\nu$ is a vector with two components, $e_1$ and $e_2$, $p_\nu$ contains $p_1$ and $p_2$ etc.

The telescope and the atmosphere will affect a point source image in two ways. First, there is the general smearing of the image caused by seeing or telescope optics (the smear term). Then there is the anisotropy caused largely by the telescope's non-axis symmetric point spread function (PSF, the shear term). The correction for these two effects for point sources is, somewhat counterintuitively, well approximated by subtracting the product of the smear polarizability $P_{{\rm sm},\nu\nu}$ for the target (this is derived from various moments of the image of the source) and $p_\nu$, a measure of PSF anisotropy at the position of the source on the image. To measure this, we measure $p_\nu$ for stars across the image and then determine how this parameter changes across the image (which we will call $p_{\nu,\,\rm smooth}$). We use two different methods, one in our tests on specific targets (see Section 3) and one in our application to the general PS1 data set (see Section 5). Once $p_\nu$ has been determined, we can measure the polarization of each object by

$$e_{\nu,\rm cor} = e_\nu - P_{{\rm sm},\nu\nu}p_{\nu,\rm smooth}, \quad (4)$$

where $p_{\nu,\,\rm smooth}$ is some smoothed function of the $p_\nu$ values across the image.

However, this is not sufficient to correctly determine the anisotropy if the object is two blended point sources, as there may be significant higher order moments. Here, an additional term called $\alpha$ is required. This was introduced by Hoekstra et al. (2005) and is an additional correction required for an object that potentially consists of two blended point sources. This modifies equation (4) to become

$$e_{\nu,\rm cor} = e_\nu - P_{{\rm sm},\nu\nu}p_{\nu,\rm smooth} - \alpha\sqrt{p_1^2 + p_2^2}. \quad (5)$$

This latter $\alpha$ term is a function of separation and flux ratio. Since these cannot be independently determined for a blended binary with no additional high-resolution imaging, $\alpha$ must be fitted as a free parameter for each object (note that it is a *per object* parameter, not a *per image* parameter). We will return to how to fit this parameter later.

For a true marginally blended binary, the ellipticity should be a function of seeing. Hence, the various values of $e_{\nu,\,\rm cor}$ are used to constrain a fit of $e_\nu$ as a function of seeing. The ellipticity is then measured at a reference seeing value for comparison with other objects.

The mathematical techniques for measuring the shapes of objects are comprehensively laid out in appendix A of Hoekstra et al. (1998). Terziev et al. (2013) repeat the relevant terms for measuring stellar shapes [albeit with an error in their equation 6 – see equation 20 of Hoekstra et al. (1998) for the correct term].

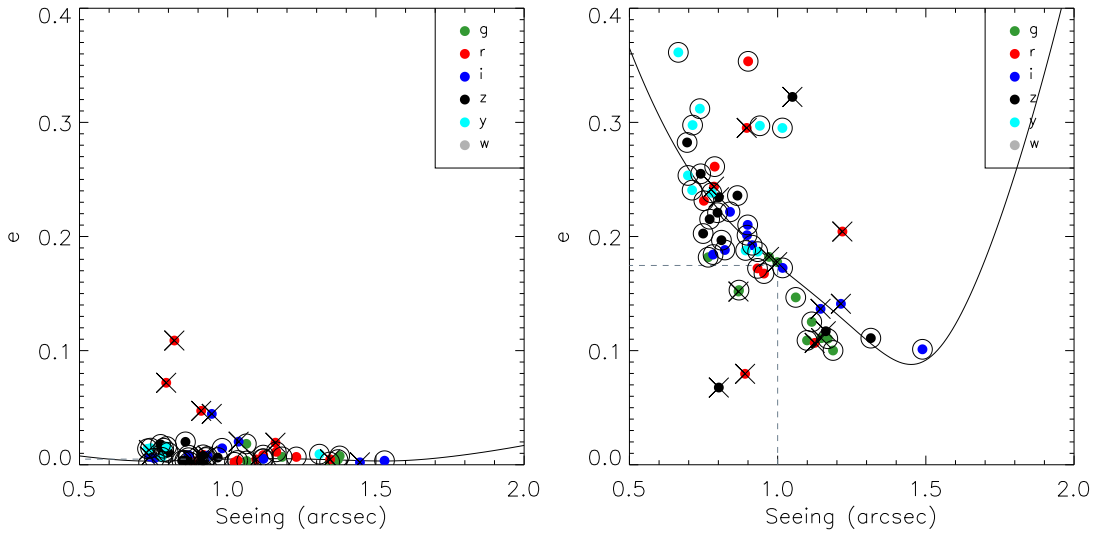


**Figure 1.** Left: the single star PTF22.415.ps, right: the 0.84 arcsec binary PTF23.553. Points with circles around them were images used for the fits for each object. Points with crosses through them were excluded due to chip gaps, streaks due to bright stars or high polarizability ($p > 3$). The dashed line marks the predicted ellipticity at a seeing of 1 arcsec.

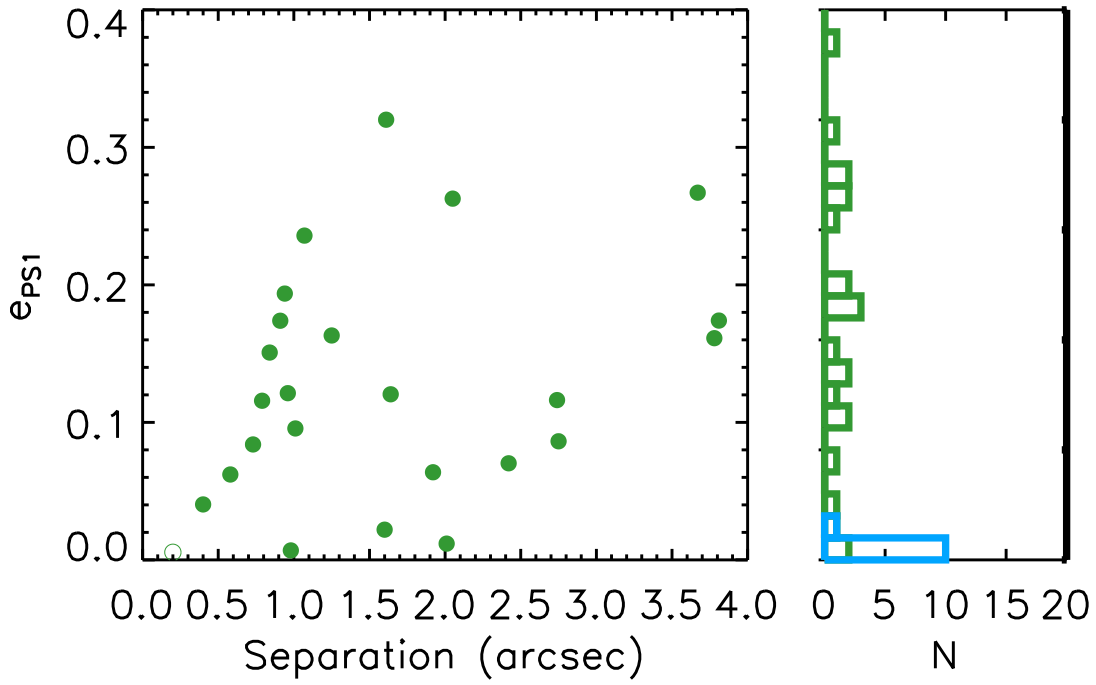


**Figure 2.** Left: the measured ellipticities at our reference seeing of 1 arcsec for binaries in the test sample of Terziev et al. (2013). The open circle is an object with a very small separation that Terziev notes would not have affected the ellipticity measurement. Right: a histogram of these ellipticities for binaries (green) and single stars (blue). Note the one binary at a separation of 2 arcsec that has a low ellipticity. This has the smallest flux ratio in the sample at 0.04.

## 3 TESTING OF PS1 IMAGES

We first applied this technique to PS1 images using the same test sample as Terziev et al. (2013). This sample has been followed up with AO imaging, meaning any of these objects that are binaries with separations down to a few tenths of an arcsecond will have been identified. Hence, we can use this sample to measure how well our method detects real astronomical binaries and how often single stars are falsely identified as binaries.

We began by extracting 10 arcmin $\times$10 arcmin images for each of the 44 objects in the Terziev sample from the PS1 postage stamp server. We requested all single-epoch 'warp' images (single epoch images re-registered to a fixed R.A. and Dec. grid with 0.25 arcsec pixels) for all filters (the standard $g_{P1}$, $r_{P1}$, $i_{P1}$, $z_{P1}$, $y_{P1}$ filters plus the wider $w_{P1}$ filter used for asteroid searches; Tonry et al. 2012) and also extracted the pixel masks for each warp. We then ran the SExtractor software package (Bertin & Arnouts 1996) on the image to identify sources in each image and to measure their flux, R.A. and Dec., and CCD $X$ and $Y$ positions along with the flags measured by SExtractor. Note that we effectively turned off SExtractor deblending by setting the deblending contrast ratio DEBLEND_MINCONT to 0.5, to avoid the centroids reported by

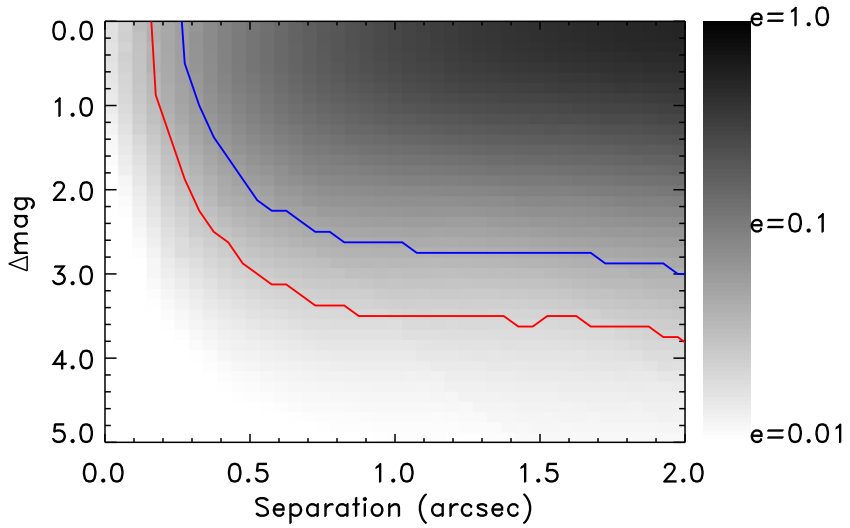


**Figure 3.** The measured ellipticities of a series of simulated binaries with varying flux ratio and separation. The red line marks the flux ratio at each separation where the measured ellipticity of the binary is above 0.02 (our chosen limit) and the blue line marks a more conservative $e = 0.04$ limit.

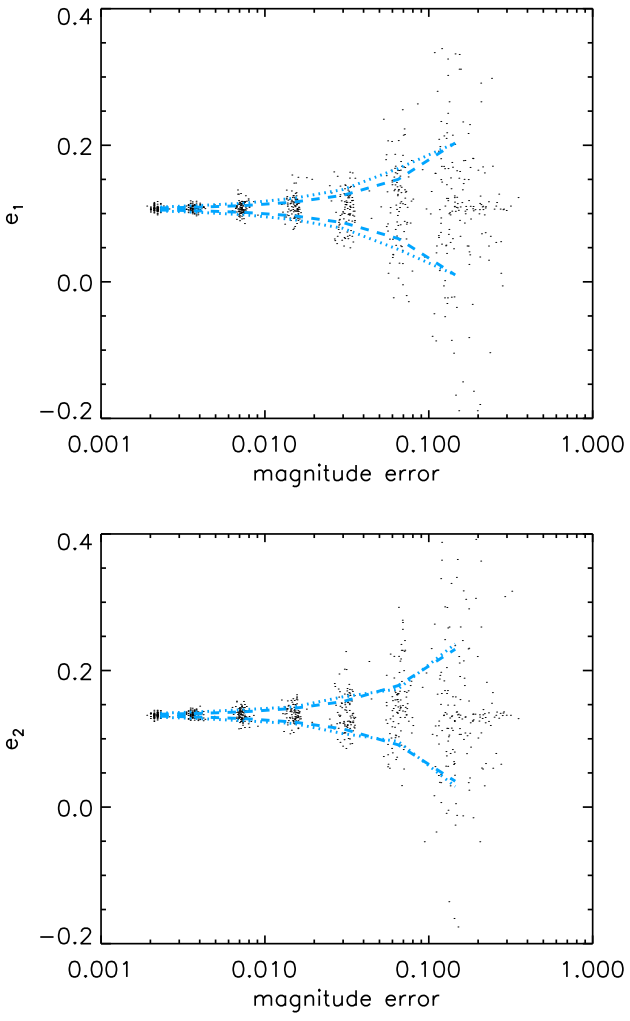


**Figure 4.** The individual ellipticity measurements, uncorrected for image anisotropy, for the same stellar image with different photon noise levels. The dotted line represents a robust (1.48 median square deviations) measure of the spread of ellipticities in each magnitude error bin and the dashed line represents our $\sigma_e = \frac{2}{3}\sigma_{\rm mag}$ fit.

SExtractor for blended objects from jumping around due to variations in seeing (being resolved in some images and not in others). The PS1 pixel mask was used to create a SExtractor weighting map excluding regions that fell on chip gaps or streaks from the removal of bright stars. We then extracted cutout images that were five times the measured full width at half-maximum (FWHM, available in the image headers) for each source on each image. We used the area at a distance of 4–5× FWHM to define our sky annulus, setting the sky value to be the median in this region. After subtracting the sky, we measured the image parameters described in Terziev et al. (2013) and Hoekstra et al. (2005), namely $e_\nu$, $p_\nu$ and $P_{\nu\nu}$ in a region within 4×FWHM of the SExtractor reported centroid. Our weighting function $W$ was a Gaussian centred on the position of the object with a standard deviation of FWHM/2.35. This is simply the width of the seeing PSF and is substantially narrower than the weighting functions used for extragalactic weak lensing surveys as galaxies have significantly more flux away from their core than stars. This value was chosen as it was found that a larger choice meant that low significance detections were vulnerable to sky noise away from the object's position. The number of pixels in the corresponding region of the pixel mask image that were flagged as gaps or streaks were also counted. This process was repeated, so we had positions, S/N estimates, image flags and shape parameters for each object on each image.

On each image, we then selected reference stars that had an S/N>10, had no SExtractor flags set, did not fall in gaps or streaks on the image, were classified by SExtractor as having a >80 per cent probability of being a star and had values of $p_1$ and $p_2$ that were less than 3 standard deviations from the median $p_1$ and $p_2$ images on that particular image. This last cut was to prevent objects with very high $p_\nu$ values from dominating our estimates of distortion across the image. Each image was required to have 10 or more reference stars meeting these conditions, otherwise it was not used in subsequent analysis. For each reference star, we measured the $p_1$ and $p_2$ parameters. We then fitted a second-order 2D polynomial for both $p_1$ and $p_2$ using the MPFIT2DFUN routine (Markwardt 2009). We found that for larger images third-order terms also become significant,

$$p_{\nu,\rm smooth} = c_{\nu,0} + c_{\nu,1}y + c_{\nu,2}x + c_{\nu,3}y^2 + c_{\nu,4}xy + c_{\nu,5}x^2. \quad (6)$$

**Table 1.** A list of objects detected with an ellipticity at the reference seeing greater than 0.02 and more significant than $4\sigma$. The column 'Good' states if we believe this to be a believable fit or not, 'Fig.' shows the figure number the object appears in and 'Known' lists if the object is a previously known binary.

| Name | $e_{\rm PS1}$ | Good | Fig. | Known | Notes |
|---|---|---|---|---|---|
| 2MASSW J1421314+182740 | $0.023 \pm 0.002$ | N | | N | Affected by nearby star. |
| 2MASSI J1426316+155701 | $0.023 \pm 0.001$ | Y | 5 | Y | Recovery of known binary. |
| SIPS J1632−0631 | $0.024 \pm 0.002$ | N | | N | No consistent ellipticity. |
| 2MASSI J0835425−081923 | $0.025 \pm 0.002$ | N | | N | Strongly affected by one outlier measurement. |
| 2MASS J17343053−1151388 | $0.031 \pm 0.001$ | N | | N | Strongly affected by one outlier measurement. |
| 2MASS J17461199+5034036 | $0.035 \pm 0.008$ | N | | N | Strongly affected by one outlier measurement. |
| 2MASS J18000116−1559235 | $0.036 \pm 0.003$ | N | | N | Crowded field. |
| Kelu-1 | $0.041 \pm 0.003$ | Y | 5 | Y | Recovery of known binary. |
| LHS 2930 | $0.042 \pm 0.001$ | N | | N | Saturated. |
| 2MASSW J2206228−204705 | $0.042 \pm 0.001$ | Y | 6 | Y | Recovery of known binary. |
| 2MASS J17312974+2721233 | $0.047 \pm 0.001$ | N | | N | Affected by nearby star. |
| 2MASS J09153413+0422045 | $0.052 \pm 0.006$ | Y | 6 | Y | Recovery of known binary. |
| 2MASS J05301261+6253254 | $0.057 \pm 0.006$ | N | | N | Strongly affected by one outlier measurement. |
| WISEPA J061135.13−041024.0 | $0.063 \pm 0.016$ | Y | 7 | Y | Recovery of known binary. |
| WISE J180952.53−044812.5 | $0.065 \pm 0.009$ | Y | 10 | N | Discovery. |
| 2MASS J17072343−0558249 | $0.065 \pm 0.001$ | Y | 7 | Y | Recovery of known binary. |
| 2MASS J05431887+6422528 | $0.072 \pm 0.003$ | Y | 10 | N | Discovery. |
| 2MASS J11000965+4957470 | $0.099 \pm 0.015$ | N | | N | Extremely noisy detections CHECK. |
| SIMP J1619275+031350 | $0.125 \pm 0.025$ | Y | 8 | Y | Recovery of known binary. |
| LP 44−334 | $0.130 \pm 0.001$ | Y | 12 | N | Discovery. |
| WISE J072003.20−084651.2 | $0.138 \pm 0.001$ | N | | N | Saturated. |
| 2MASS J19303829−1335083 | $0.141 \pm 0.001$ | N | | N | Saturated. |
| DENIS-P J220002.05−303832.9 | $0.214 \pm 0.008$ | Y | 8 | Y | Recovery of known binary. |
| 2MASS J15500845+1455180 | $0.231 \pm 0.011$ | Y | 9 | Y | Recovery of known binary. |
| G 196−3B | $0.317 \pm 0.027$ | N | | N | Affected by nearby star. |
| LP 412−31 | $0.385 \pm 0.001$ | N | | N | Strongly affected by one outlier measurement. |
| DENIS J020529.0−115925 | $0.785 \pm 0.160$ | N | 9 | Y | Strongly affected by one outlier measurement. |

**Table 2.** A list of objects that did not have ellipticity at the reference seeing greater than 0.02 and more significant than $4\sigma$. A full version of this table will be available online

| Name | R.A. | Dec. | $e_{\rm PS1}$ | $e_1$ | $e_2$ |
|---|---|---|---|---|---|
| SDSS J000112.18+153535.5 | 00:01:12.28 | +15:35:33.7 | $0.338 \pm 0.111$ | $-0.181 \pm 0.111$ | $0.286 \pm 0.111$ |
| 2MASSW J0015447+351603 | 00:15:44.82 | +35:15:59.9 | $0.005 \pm 0.002$ | $0.003 \pm 0.003$ | $0.005 \pm 0.002$ |
| 2MASS J00192626+4614078 | 00:19:26.40 | +46:14:06.8 | $0.001 \pm 0.0$ | $0.0 \pm 0.0$ | $0.0 \pm 0.0$ |
| BRI 0021−0214 | 00:24:24.58 | −01:58:18.4 | $0.006 \pm 0.001$ | $-0.001 \pm 0.0$ | $-0.005 \pm 0.001$ |
| LP 349−25 | 00:27:56.31 | +22:19:30.6 | $0.002 \pm 0.0$ | $0.001 \pm 0.0$ | $-0.002 \pm 0.0$ |
| PSO J007.9194+33.5961 | 00:31:40.65 | +33:35:45.9 | $0.133 \pm 0.099$ | $-0.08 \pm 0.099$ | $-0.106 \pm 0.099$ |

We then used equation (4) to remove most of the image anisotropy. We do not do the final correction for the $\alpha$ parameter introduced by Hoekstra et al. (2005) at this stage, as this is a *per object* rather than a *per image* parameter.

The detections for our target object across each image were then collected together and a fit for the variation with seeing and the $\alpha$ correction were applied as

$$e_{{\rm fit},\nu} = c_{{\rm fit},0} + c_{{\rm fit},1}{\rm FWHM} + c_{{\rm fit},2}{\rm FWHM}^2 + \alpha\sqrt{p_1^2 + p_2^2}. \quad (7)$$

In doing this fit, we exclude any detection with an ellipticity greater than 1, which has $\sqrt{p_1^2 + p_2^2} > 3$, which has a chip gap or streak within 4 ×FWHM or which is detected at an S/N less than 15. This latter cut is more stringent than our cut for reference stars and is included to prevent individual, low-significance detections in good seeing from adversely affecting our fits. Hoekstra et al. (2005) suggest that the typical value of $\alpha$ is around 0.6 times the ellipticity at the reference seeing value for the object. To prevent the value of $\alpha$ becoming too large, we carried out an initial fit where $\alpha$ was set to zero but $c_{{\rm fit},0}$, $c_{{\rm fit},1}$ and $c_{{\rm fit},2}$ were allowed any value. We then determined $e_{{\rm fit},\nu}$ at a reference seeing of 1 arcsec from our initial fit ($e_{{\rm fit},\nu,{\rm ref}}$) and then undertook a second fit where we limited $\alpha$ to be $-e_{{\rm fit},\nu,{\rm ref}} < \alpha < e_{{\rm fit},\nu,{\rm ref}}$ again also fitting for $c_{{\rm fit},0}$, $c_{{\rm fit},1}$ and $c_{{\rm fit},2}$. Once this was done, we recalculated the value of $e_{{\rm fit},\nu,{\rm ref}}$ for our new fit and used it as a diagnostic for stellar binarity. Only objects with six or more detections were considered for subsequent analysis. We found this threshold was the minimum possible before we became swamped with false detections from poor fits.

### 3.1 Results of the Terziev test sample

40 of the 44 objects in the Terziev test sample had a sufficient number of measurements for fits to be performed. Of these, 12 were known single stars and 28 binaries (with one having a separation which Terziev et al. 2013 notes is too small to affect the ellipticity measurements). Fig. 1 shows two objects, one a single star and one a 0.84 arcsec binary. It is clear that the binary has both a higher ellipticity at the reference seeing and rising ellipticity as image quality improves. Fig. 2 shows the ellipticities at our reference

**Table 3.** The individual ellipticity polarizations, implied binary orientation and literature position angles for our sample of recovered binaries.

| Name | $e_1$ | $e_2$ | Implied alignment | Literature separation | Literature P.A. |
|---|---|---|---|---|---|
| 2MASSI J1426316+155701 | $-0.023 \pm 0.001$ | $0.005 \pm 0.001$ | N–S | 0.32 arcsec | $343^{\circ a}$ |
| Kelu-1 | $-0.002 \pm 0.002$ | $-0.041 \pm 0.003$ | NE–SW | 0.39 arcsec | $255^{\circ b}$ |
| 2MASSW J2206228−204705 | $0.042 \pm 0.001$ | $0.006 \pm 0.001$ | N–S[c] | 0.14 arcsec | $216^{\circ b}$ |
| 2MASS J09153413+0422045 | $-0.001 \pm 0.005$ | $-0.052 \pm 0.006$ | N–S | 0.73 arcsec | $205^{\circ d}$ |
| WISEPA J061135.13−041024.0 | $-0.044 \pm 0.016$ | $-0.046 \pm 0.016$ | NNE–SSW | 0.38 arcsec | $33^{\circ e}$ |
| 2MASS J17072343−0558249 | $-0.007 \pm 0.001$ | $-0.065 \pm 0.001$ | N–S | 1.00 arcsec | $35^{\circ d}$ |
| SIMP J1619275+031350 | $0.062 \pm 0.025$ | $-0.108 \pm 0.025$ | ENE–WSW | 0.69 arcsec | $71^{\circ f}$ |
| DENIS-P J220002.05−303832.9 | $-0.211 \pm 0.008$ | $-0.036 \pm 0.009$ | N–S | 1.09 arcsec | $177^{\circ g}$ |
| 2MASS J15500845+1455180 | $-0.229 \pm 0.011$ | $-0.030 \pm 0.011$ | N–S | 0.91 arcsec | $17^{\circ h}$ |
| DENIS J020529.0−115925 | $0.785 \pm 0.161$ | $-0.004 \pm 0.161$ | E–W | 0.29 arcsec | $246^{\circ ij}$ |

[a]Konopacky et al. (2010).
[b]Dupuy and Liu orbital monitoring (Dupuy & Liu in preparation).
[c]Whilst this object has reference seeing ellipticities that suggest an E–W alignment, inspection of the actual fit (Fig. 6) shows four points with excellent seeing with −ve $e_2$ values, suggesting N–S.
[d]Reid et al. (2006).
[e]Gelino et al. (2014).
[f]Artigau et al. (2011).
[g]Burgasser & McElwain (2006).
[h]Burgasser et al. (2009).
[i]Bouy et al. (2003).
[j]Spurious ellipticity estimate due to exceptionally good seeing on a handful of measurements.

seeing of 1 arcsec for these 40 objects from the Terziev et al. (2013) sample. All but two binaries have ellipticities higher than 0.02 (the cutoff value Terziev suggests for PTF). Of these two binaries, one has a very small separation and the other has a flux ratio of 0.04, the smallest in the Terziev sample. Terziev's measurement of the ellipticity of this object was similarly low at 0.014. This shows that we are able to reliably recover known binaries in the Terziev sample without producing a large number of false positives.

Terziev et al. (2013) use the absolute magnitude of the slope of the ellipticity/seeing relation divided by the reference ellipticity as a measure of binary separation. We found a correlation between this statistic and binary separation but the scatter on the relation between the two was too large for it to act as a useful diagnostic.

### 3.2 Testing with simulated data

To test our ability to probe binaries with different flux ratios and separations, we performed a series of simulations. We selected one single, low ellipticity star from the Terziev sample and injected a copy of it at different separations and flux ratios. The seeing of the image chosen was 0.97 arcsec, close to our reference seeing of 1 arcsec. We then ran our shape measurement code on these simulated binaries to determine the ellipticities across our parameter range. The resulting ellipticities are shown in Fig. 3 suggesting that binaries wider than 0.4 arcsec and with magnitude differences less than 3 will be readily identifiable with our method.

To test the accuracy of our ellipticity measurements, we took a well-exposed stellar image with seeing of approximately 1 arcsec, multiplied it by a factor less than 1 to reduce its brightness and added Poisson noise to it. This was then injected onto a blank region of a PS1 image. We repeated this process with different multiplying factors to produce a series of objects with a range of detection significances (and hence different errors on the measured magnitude of the star in SExtractor). We then ran each simulated image through our process and noted the measured magnitude error and ellipticities for each simulated object. Fig. 4 shows how the range of measured ellipticities increases with increasing magnitude error. We estimated the error on the ellipticity by dividing the data into seven bins and finding in each the median absolute deviation from the overall median value of each ellipticity parameter. We use this technique to prevent our error estimates being driven by a handful of outliers. This median absolute deviation was multiplied by a factor of 1.48 to produce a robust estimate of the typical standard deviation of ellipticity measurements. We found that the error in each bin was well fitted by

$$\sigma_e = \frac{2}{3}\sigma_{\rm mag} \tag{8}$$

and have used this form in the rest of our analysis.

## 4 SEARCHING FOR BINARY BROWN DWARFS

We applied our binary search technique to a sample of ultracool dwarfs in the solar neighbourhood. To do this, we searched a list of objects later than M6 compiled by W. Best (see Best et al. 2017, for details) for objects with distance estimates less than 30 pc and a total Pan-STARRS 1 S/N ratio over all epochs in either $z_{\rm P1}$ or $y_{\rm P1}$ greater than 15. This left us with 664 objects, all north of $\delta = -30^{\circ}$. We extracted postage stamp images from the PS1 postage stamp server for all objects. These images were from the PV3 processing run, were 'warp' images (i.e. resampled on a regular grid of pixels aligned with the R.A. and Dec. axes) and covered 10 arcmin × 10 arcmin each. As we used individual epoch 'warp' images calculating stellar centroid positions on each, we are not affected by centroid offsets caused by proper motion. We also downloaded the corresponding mask images to allow us to flag objects that lay close to a chip gap or image streak. On each image, we then ran SExtractor and followed our previously described reference star selection technique. We then corrected the ellipticity parameters for every object on the image using our smoothed estimate of the image anisotropy (using equations 4 and 5).

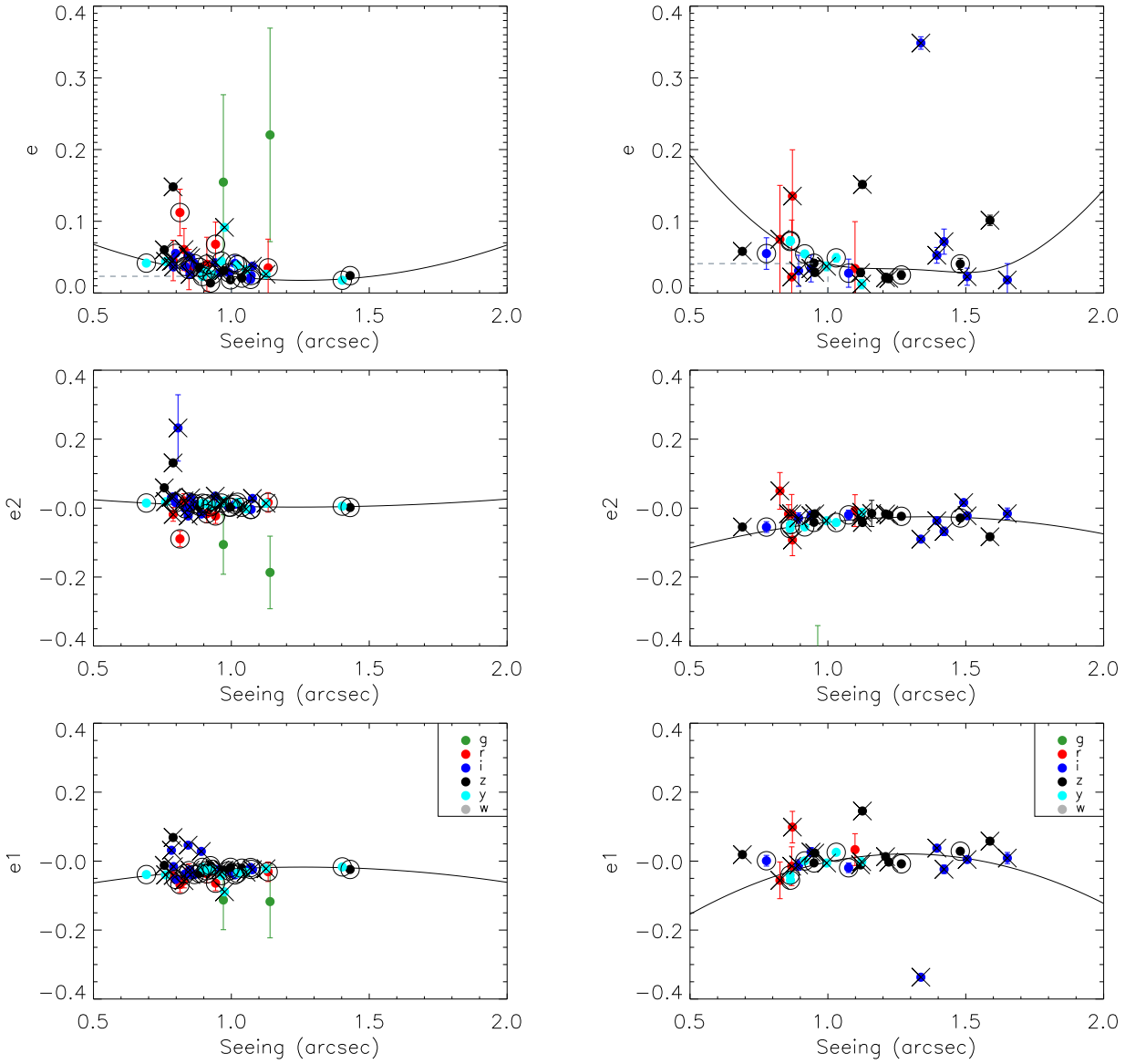


**Figure 5.** Ellipticity measurements and fits for the known binaries 2MASSI J1426316+155701 (left) and Kelu-1 (right). The top plot shows the total ellipticity, the middle plot the '×' polarization $e_2$ and the bottom plot the '+' polarization $e_2$. Points used in the second-order polynomial fits are outlined by a circle and those rejected for data quality reasons are crossed out. Note that due to the coordinate system of the postage stamps used, a positive $e_2$ is an elongation in the NW–SE direction and a positive $e_1$ is an elongation along the $x$ (i.e. R.A.) axis.

For each of our targets, we selected any individual epoch detection with S/N>15. We then fitted second-order polynomials to both the corrected values of $e_1$ and $e_2$ using a least-squares fitting method where the errors on each ellipticity measurements were determined using equation (8). We then estimated the total ellipticity value at a seeing of 1 arcsec and propagated the errors from our covariance matrix to determine a standard deviation for this value.

Out of a total of 664 objects in our input sample, 282 had six or more images with a sufficient number of reference stars, where the target was detected with sufficient significance and where the target was not affected by chip gaps or streaks. We then selected objects with a reference ellipticity greater than 0.02 and with that ellipticity being more significant than $4\sigma$. Table 1 lists these 27 objects and our evaluation of them. Table 2 lists objects that did not pass our ellipticity cuts either due to a low ellipticity measurement or a low measurement significance.

### 4.1 Notes on previously known binaries

In this section, we discuss previously known binaries that we have recovered. Note that due to the pixel coordinates of our images (increasing $x$ coordinate with decreasing R.A., increasing $y$ with increasing Dec.), a positive value of $e_1$ will represent an elongation in the R.A. direction and a positive value of $e_2$ will be derived from an elongation in the north-east to south-west direction. This means that the right-hand side of the $e_2$ equation shown in equation (3) is multiplied by a factor of $-1$. We summarize our alignment estimates and the literature position angles in Table 3.

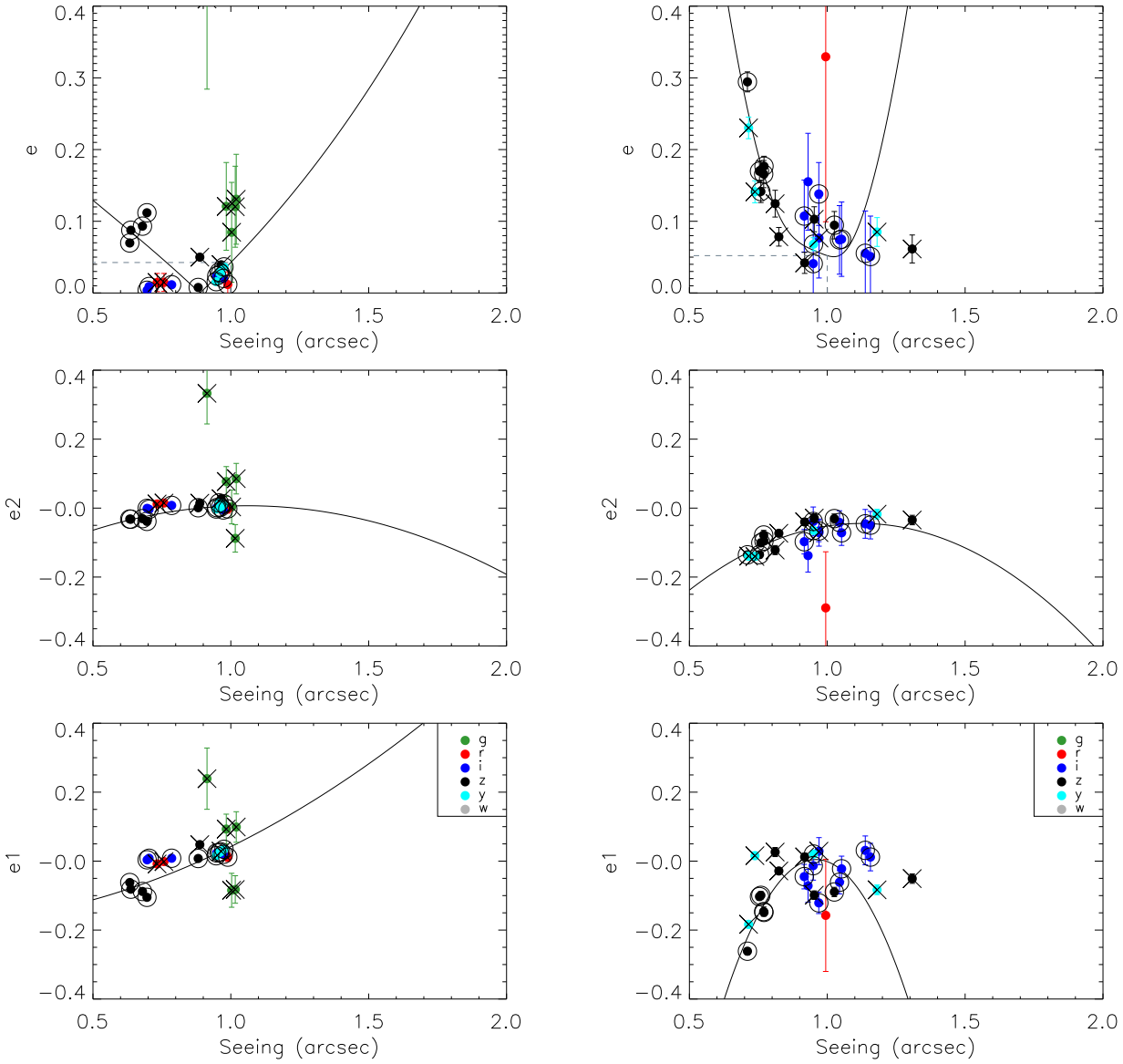


**Figure 6.** Ellipticity measurements and fits for the known binaries 2MASSW J2206228−204705 (left) and 2MASS J09153413+0422045 (right). The top plot shows the total ellipticity, the middle plot the '×' polarization $e_2$ and the bottom plot the '+' polarization $e_2$. Points used in the second-order polynomial fits are outlined by a circle and those rejected for data quality reasons are crossed out. Note that due to the coordinate system of the postage stamps used, a positive $e_2$ is an elongation in the NW–SE direction and a positive $e_1$ is an elongation along the $x$ (i.e. R.A.) axis.

#### *4.1.1 2MASSI J1426316+155701*

This M8.5+L1 binary was discovered by Close et al. (2003) having a separation of 0.152 ±0.006 arcsec and position angle of 344.1 ±0.°7 in 2001 June. Later observations by Konopacky et al. (2010) from 2009 March give a separation of 0.3226 ±0.0006 arcsec and position angle of 343.8 ±0.°08, suggesting an edge-on orbit. We find that our fit (see Fig. 5) is dominated by a negative $e_1$, suggesting an elongation along the north–south axis, in good agreement with the previous position angles.

#### *4.1.2 Kelu-1*

This L1.5-L3+L3-L4.5 binary was discovered by Liu & Leggett (2005) and has been monitored by M. Liu and T. Dupuy ever since (Dupuy & Liu in preparation). During PS1 observations, this binary would have had a separation of around 0.39 arcsec and a position angle of 255° (Dupuy et al. in preparation). Our fit shows a consistently negative $e_2$ that suggests an elongation in the NE–SW direction (see Fig. 5).

#### *4.1.3 2MASSW J2206228−204705*

Discovered by Close et al. (2003), this M8+M8 binary has been monitored by M. Liu and T. Dupuy (Dupuy & Liu in preparation) since its initial identification. Our fit (see Fig. 6) is heavily driven by four $z_{P1}$ observations taken on 2010 November 10 with very good seeing (0.6–0.7 arcsec). The main characteristic of the fit is a highly negative value of $e_1$ (elongation along the N–S axis) and a slightly negative value of $e_2$ (suggesting a tilt towards an NE–SW

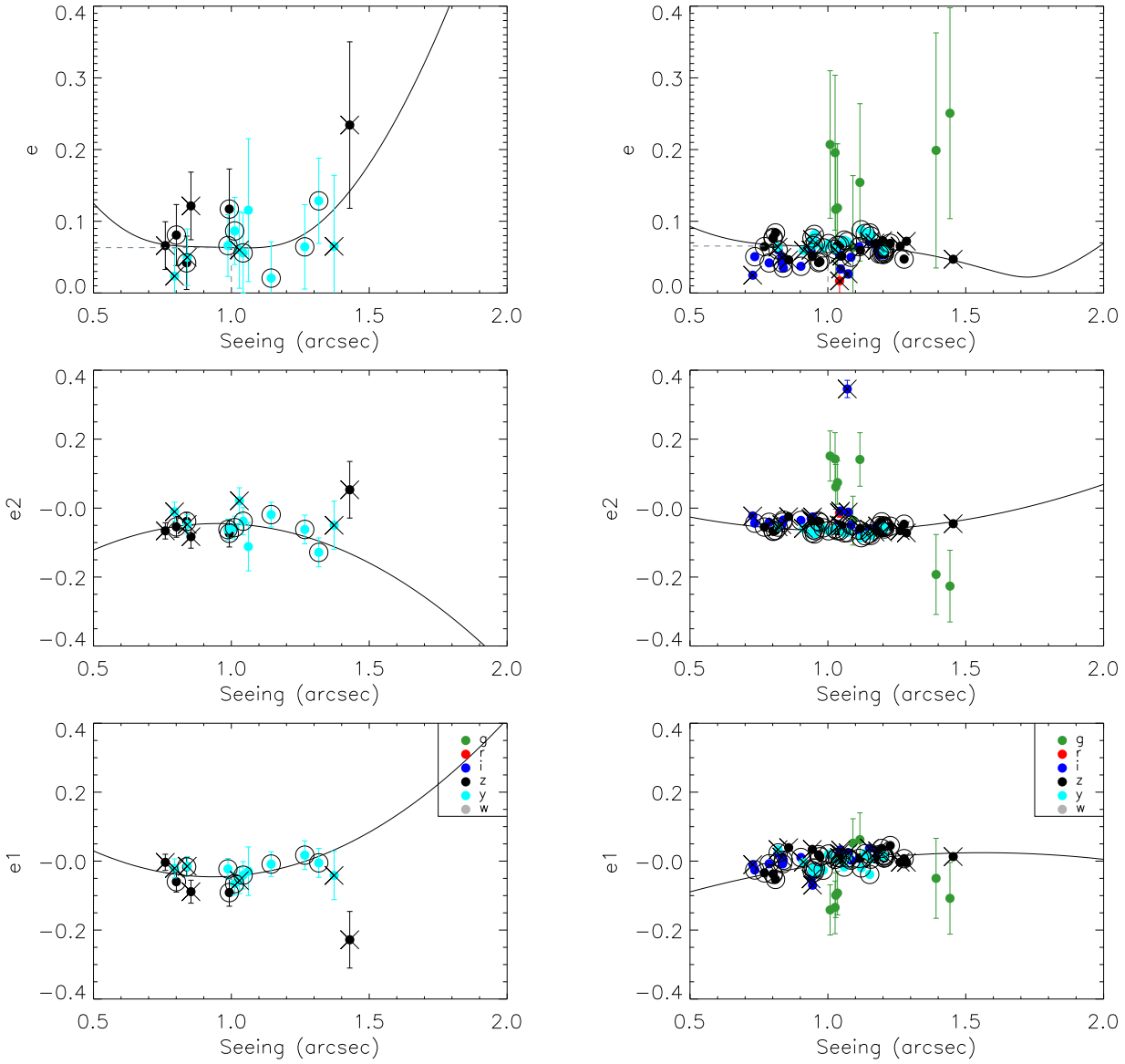


**Figure 7.** Ellipticity measurements and fits for the known binaries WISEPA J061135.13−041024.0 (left) and 2MASS J17072343−055824 (right). The top plot shows the total ellipticity, the middle plot the '×' polarization $e_2$ and the bottom plot the '+' polarization $e_2$. Points used in the second-order polynomial fits are outlined by a circle and those rejected for data quality reasons are crossed out. Note that due to the coordinate system of the postage stamps used, a positive $e_2$ is an elongation in the NW–SE direction and a positive $e_1$ is an elongation along the $x$ (i.e. R.A.) axis.

alignment). The orbital solution for 2MASSW J2206228−204705 suggests a separation of 0.139 arcsec and a position angle of 216° (Dupuy et al. in preparation), in agreement with our suggested alignment. It should be noted that this binary is much tighter than we would normally expect to detect, but it appears that we are able to detect this due to a single night of exceptional data.

#### *4.1.4 2MASS J09153413+0422045*

This L7+L7 binary was discovered by Reid et al. (2006) as having a separation of 0.73 arcsec and position angle of 205°. Our solution (see Fig. 6) results in a highly negative value of $e_1$ and a smaller but negative value of $e_2$. This suggests a binary primarily elongated along the N–S axis but tilted towards the NE–SW direction, in agreement with Reid et al. (2006)'s position angle.

#### *4.1.5 WISEPA J061135.13−041024.0*

Discovered by Gelino et al. (2014), this L/T transition (L9+T1.5) binary has a separation of 0.384 arcsec and a position angle of 32°.5. Our fit (see Fig. 7) is dominated by a negative value of $e_2$ (suggesting an NE–SW alignment) with a slightly negative value of $e_1$, suggesting a slight elongation in $y$. This is consistent with the known position angle of the binary.

#### *4.1.6 2MASS J17072343−055824*

This known M9+L3 (Reid et al. 2006) binary had a separation of 1.04 ±0.04 arcsec, P.A.=145 ±2° in 2003 March (McElwain & Burgasser 2006). This is significantly discrepant from our negative value of $e_2$, suggesting a position angle of around 45°

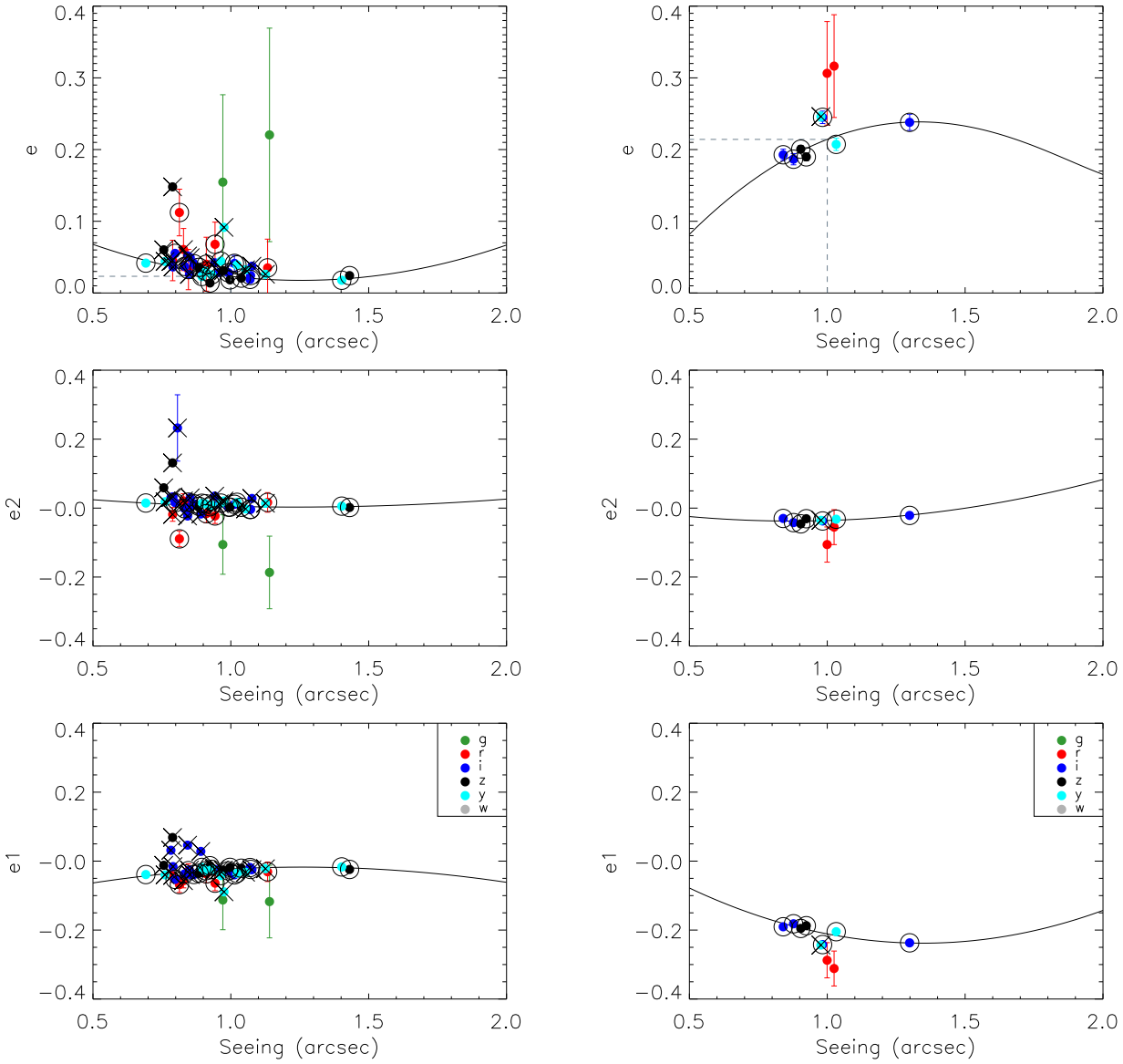


**Figure 8.** Ellipticity measurements and fits for the known binaries SIMP J1619275+031350 (left) and DENIS-P J220002.05−303832.9 (right). The top plot shows the total ellipticity, the middle plot the '×' polarization $e_2$ and the bottom plot the '+' polarization $e_2$. Points used in the second-order polynomial fits are outlined by a circle and those rejected for data quality reasons are crossed out. Note that due to the coordinate system of the postage stamps used, a positive $e_2$ is an elongation in the NW–SE direction and a positive $e_1$ is an elongation along the $x$ (i.e. R.A.) axis.

(see Fig. 7). An inspection of the PS1 images along with an image from the Vista Hemisphere Survey (Cross et al. 2012) confirms that the binary is aligned with a position angle of roughly 45°. McElwain & Burgasser (2006)'s discovery image shows no additional object that could affect this measurement. Our position angle estimate is in much better agreement with the estimate of 35° by Reid et al. (2006).

#### *4.1.7 SIMP J1619275+031350*

Artigau et al. (2011) discovered that this object was a 0.691±0.002 arcsec T2.5+T4.0 binary. The position angle is 71.23±0.°23, in agreement with our positive value of $e_1$ and negative value of $e_2$ (see Fig. 8).

#### *4.1.8 DENIS-P J220002.05−303832.9*

This object was identified as a 1.094±0.06 arcsec, P.A.=176.7±2.°0 M9+L0 by Burgasser & McElwain (2006). This position angle agrees well with our highly negative value of $e_1$ (see Fig. 8).

#### *4.1.9 2MASS J15500845+1455180*

This object was identified as a 0.91 arcsec L3.5+L4 binary by Burgasser, Dhital & West (2009). Our recovery of this system shows a negative value of $e_1$, suggesting an elongation along the N–S axis, consistent with Burgasser et al. (2009)'s position angle of 16.6±1.°3. We detect a slight negative $e_2$ at increasing seeing (see Fig. 9). This is because our $x$ pixel number increases with decreasing R.A., meaning that a negative $e_2$ suggests a binary tilted towards the north-east.

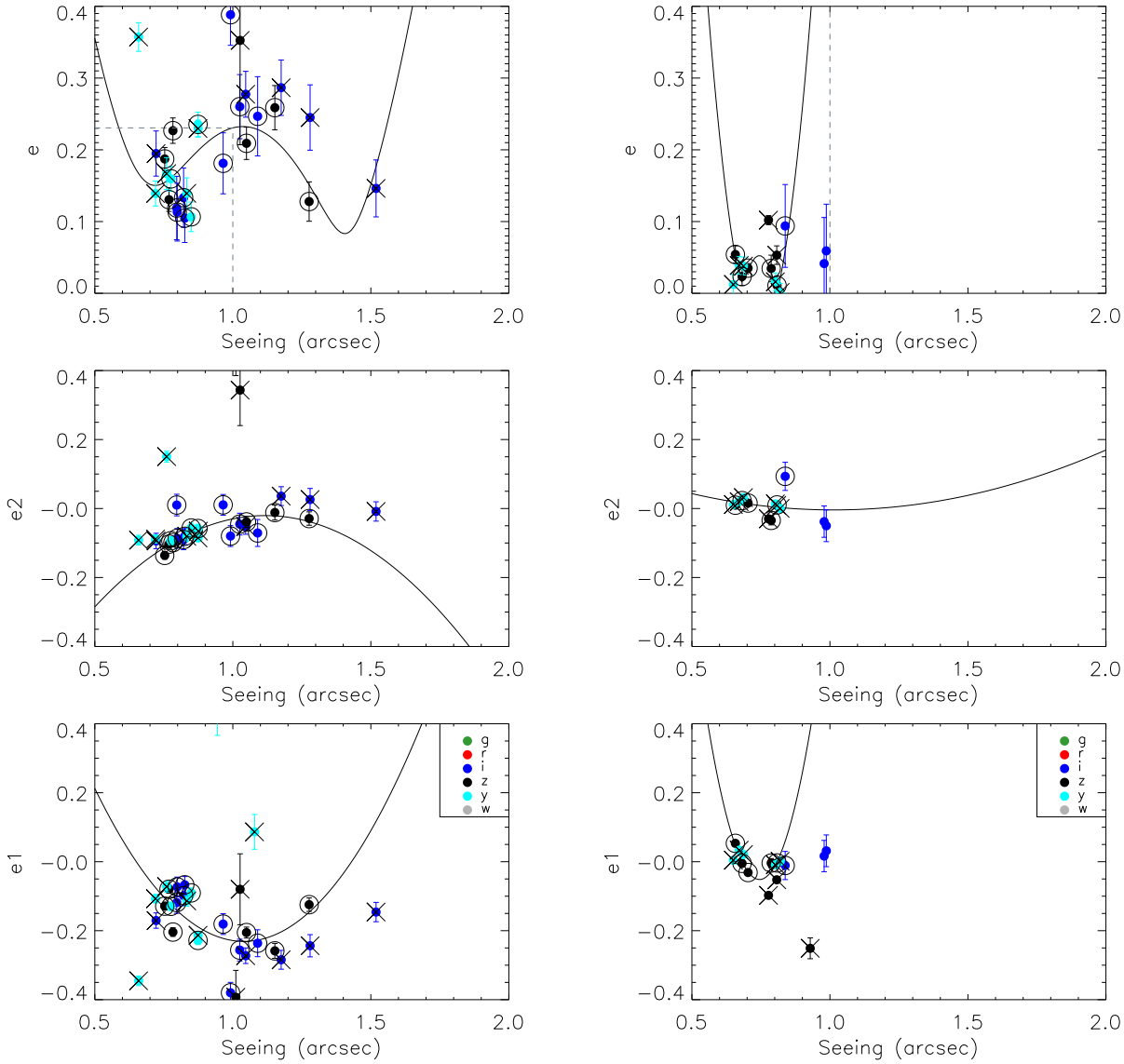


**Figure 9.** Ellipticity measurements and fits for the known binaries 2MASS J15500845+1455180 (left) and DENIS J020529.0−115925 (right). The top plot shows the total ellipticity, the middle plot the '×' polarization $e_2$ and the bottom plot the '+' polarization $e_2$. Points used in the second-order polynomial fits are outlined by a circle and those rejected for data quality reasons are crossed out. Note that due to the coordinate system of the postage stamps used, a positive $e_2$ is an elongation in the NW–SE direction and a positive $e_1$ is an elongation along the $x$ (i.e. R.A.) axis.

#### *4.1.10 DENIS J020529.0−115925*

This is an L7+L7 (Reid et al. 2006) binary detected by Bouy et al. (2003) with a separation of 0.287 ±0.005 arcsec and a position angle of 246 ±1° (see Fig. 9); however, the reference ellipticity is anomalously high. This is the result of a conspiracy of circumstances: we have very few data points, all of them at significantly better seeing than 1 arcsec. This leads to the ellipticity at the reference seeing being an extrapolation which is strongly affected by one poor data point with the worst seeing. We note that the rising $e_1$ at better seeing points to a binary is elongated along the E–W axis.

### 4.2 Newly identified binaries

#### *4.2.1 WISE J180952.53−044812.5*

WISE J180952.53−044812.5 was discovered by Mace et al. (2013), who classified it as T0.5. We identified this object as having a positive value of $e_1$ indicating an elongation in the R.A. axis (see Fig. 10). This was independently discovered as a binary by Best et al. (2017) with a separation of 0.3 arcsec and position angle of 112°. This upcoming discovery paper measures relative photometry of $\Delta J = -0.442$ ±0.059 mag and $\Delta K$=0.410 ±0.023 mag from Keck-AO observations. Note that this is a flux reversal binary with the western component brighter in $J$ and the eastern component brighter in $K$. Based on these colours and the typical colours for ultracool dwarfs in table 15 of Dupuy & Liu (2012), we estimate that the eastern component has spectral type L8-L9 and the western component is a T2-T3.

#### *4.2.2 2MASS J05431887+6422528*

This object was identified as an L1 by Reid et al. (2008). We measured a significantly positive value of $e_2$ indicating an elongation in the NW–SE direction. We observed this object on 2014 Jan 22 UT

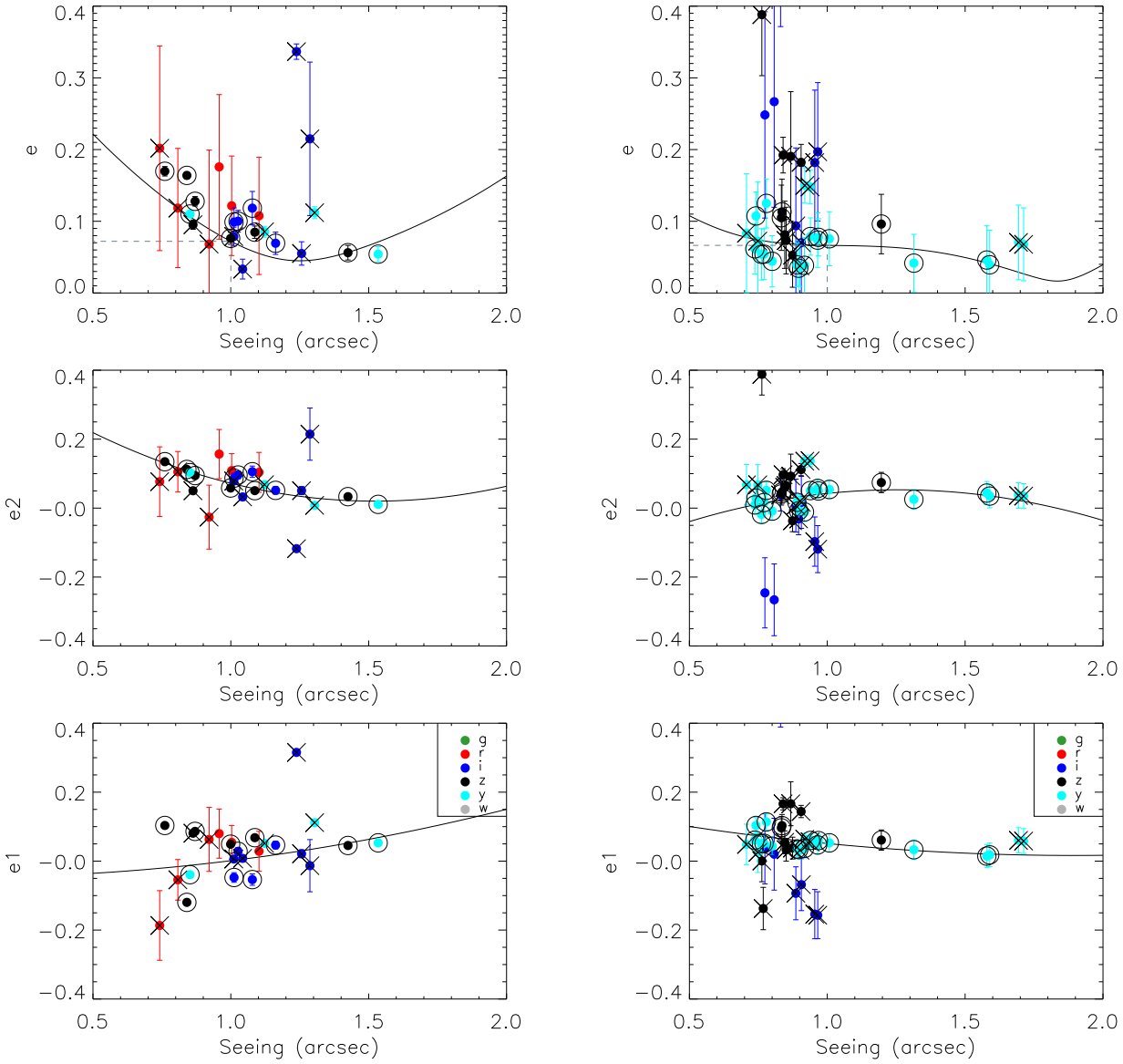


**Figure 10.** Ellipticity measurements and fits for 2MASS J05431887+6422528 (left) and WISE J180952.53−044812.5 (right). The top plot shows the total ellipticity, the middle plot the '×' polarization $e_2$ and the bottom plot the '+' polarization $e_2$. Points used in the second-order polynomial fits are outlined by a circle and those rejected for data quality reasons are crossed out. Note that due to the coordinate system of the postage stamps used, a positive $e_2$ is an elongation in the NW–SE direction and a positive $e_1$ is an elongation along the $x$ (i.e. R.A.) axis.

using the Near Infrared Camera 2 (NIRC2) imaging camera on the Keck II telescope on Mauna Kea, Hawaii. We obtained four images in the $K$ band and five images in the $J$ band, using the wide camera mode of NIRC2. We reduced the images in a standard fashion using custom IDL scripts. We constructed flat-fields from the differences of images of the telescope dome interior with and without lamp illumination. We subtracted an average bias from the images and divided by the flat-field. Then we created a master sky frame from the median average of the bias-subtracted, flat-fielded images and subtracted it from the individual reduced images. We registered and stacked the individual reduced images to form a final mosaic. We used the STARFINDER package (Diolaiti et al. 2000) that iteratively solves for both the binary parameters and an empirical image of the PSF. We determined the uncertainties in these binary parameters from the rms scatter among each data set. To correct for non-linear distortions in NIRC2, we used the calibration of (Fu et al. 2012, private communication),[1] with a corresponding pixel scale of 39.686 mas pixel$^{-1}$ and the same $+0\overset{\circ}{.}252 \pm 0\overset{\circ}{.}009$ correction for the orientation given in the NIRC2 image headers as in Yelda et al. (2010). The photometric errors are computed as the rms of individual frames, which sometimes does not fully capture systematic errors, e.g. from PSF fitting. For practical purposes, the flux ratios are more precise than the integrated-light photometry, which will be the limiting factor in the precision of the resolved photometry for the binary. Our reduced images are shown in Fig. 11. The separation and position angle measured in the $K$ band (655.37 ± 3.39 mas and 320.14 ± 0.24 deg)

[1] http://astro.physics.uiowa.edu/~fu/idl/nirc2wide/

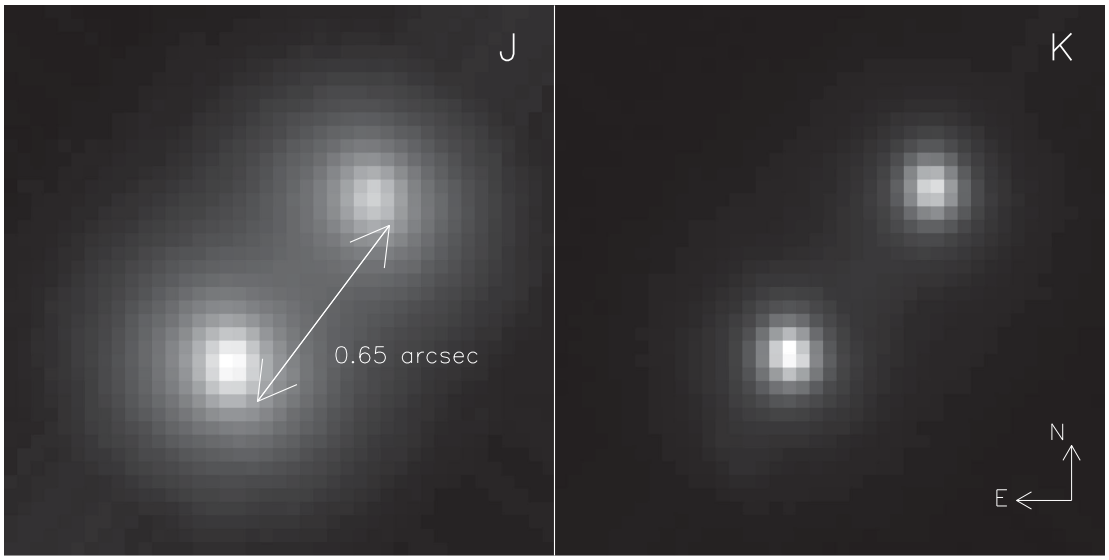


**Figure 11.** A Keck/NIRC2 image of 2MASS J05431887+6422528, we find a roughly equal-flux binary with a separation of 0.65 arcsec.

were consistent with and more precise than measured in the *J* band (656.66 ± 3.55 mas and 319.85 ± 0.36 deg). The flux ratio in the *J* band (0.284 ± 0.030 mag) is further from unity than in the *K* band (0.259 ± 0.064 mag), implying that the brighter, southeastern component is marginally bluer as expected. The integrated spectral type of L1 (Reid et al. 2008) and the small magnitude difference suggest that the components have spectral types of approximately L0.5 and L1.5.

#### *4.2.3 LP 44−334*

We identified the known M6.5 (Reid et al. 2004) LP 44−334 as having a strongly positive value of $e_2$ suggesting an elongation in the NW–SE direction (see Fig. 12). A visual inspection of the best seeing images for each PS1 band (see Fig. 13) shows that the object is almost resolved as a pair elongated in this direction. A visual inspection of the images resulted in a separation estimate of ∼0.7 arcsec with the NW component appearing to be slightly brighter.

### 4.3 Completeness and other detections

Of the 293 objects where we have enough good data for a fit, we detected every known close binary with a separation greater than 0.3 arcsec with the exception of DENIS J020529.0−115925. We have also examined the individual fits of all the known binaries with separations greater than 0.1 arcsec. Of these, we find two objects that do not have a large ellipticity at our reference seeing but which show clear trends in ellipticity at very good seeing.

#### *4.3.1 2MASSI J0746425+200032*

This L0+L1.5 Bouy et al. (2004) was discovered by Reid et al. (2001) as a 0.22 arcsec binary with a position angle of 15°. We find (see Fig. 14) that this object has a strongly negative $e_1$ in very good seeing. This suggests an elongation along the declination axis. Monitoring by M. Liu and T. Dupuy (Dupuy & Liu in preparation) suggests a position angle of around 180° at a typical PS1 epoch of 2012.0, in agreement with our measurement.

#### *4.3.2 2MASS J21522609+0937575*

This was detected as an L6+L6 binary by Reid et al. (2006) with a separation of 0.25 arcsec and a position angle of 106°. Our fit (see Fig. 14) shows a clear trend in $e_2$ to increasingly positive values, whilst $e_1$ shows little trend with the exception of one outlier point. This suggests a position angle closer to 135°, somewhat different from the measured value in Reid et al. (2006). In their table 3, Reid et al. (2006) calculate that 2MASS J21522609+0937575 is an equal-mass 0.075 $M_\odot$ assuming a 3 Gyr age. Combining these ages and Reid et al. (2006)'s separation values and a circular orbit, we derive an approximate orbital period of 38 yr. Whilst we cannot claim to have definitely detected orbital motion, an ∼30° change in the roughly 5 yr between the Reid et al. (2006) observations and our PS1 data is not unreasonable.

## 5 APPLICATION TO THE FULL PS1

We applied the methods set out above to the PS1 data base. The data base table `FORCED_WARP_LENS` includes the relevant parameters to estimate the shapes of objects and to correct for PSF anisotropy. The image moments $M_{XX}$, $M_{XY}$ and $M_{YY}$ are equivalent to the parameters $I_{11}$, $I_{12}$ and $I_{22}$, respectively. The PSF anisotropy was measured by dividing each skycell in the image into 5 arcmin×5 arcmin areas. The median image parameters of PSF stars in each region were then determined and recorded in the data base with the suffix `_PSF`. Thus, once one has calculated $e_1$ and $e_2$ from the image moments, the appropriate anisotropy correction can be made using

$$\begin{aligned} P_{\nu,\nu} &= X\nu\nu\_\mathrm{sm\_OBJ} - e\nu\_\mathrm{SM\_OBJ} \times e_\nu \\ P_{\mathrm{smooth},\nu,\nu} &= X\nu\nu\_\mathrm{sm\_PSF} - e\nu\_\mathrm{SM_{PSF}} \times e\nu\_\mathrm{PSF} \\ p_{\mathrm{smooth},\nu} &= \frac{e\nu\_\mathrm{PSF}}{P_{\mathrm{smooth},\nu,\nu}} \\ e_{\nu,\mathrm{corr}} &= e_\nu - p_{\mathrm{smooth},\nu} \times P_{\nu,\nu}. \end{aligned} \quad (9)$$

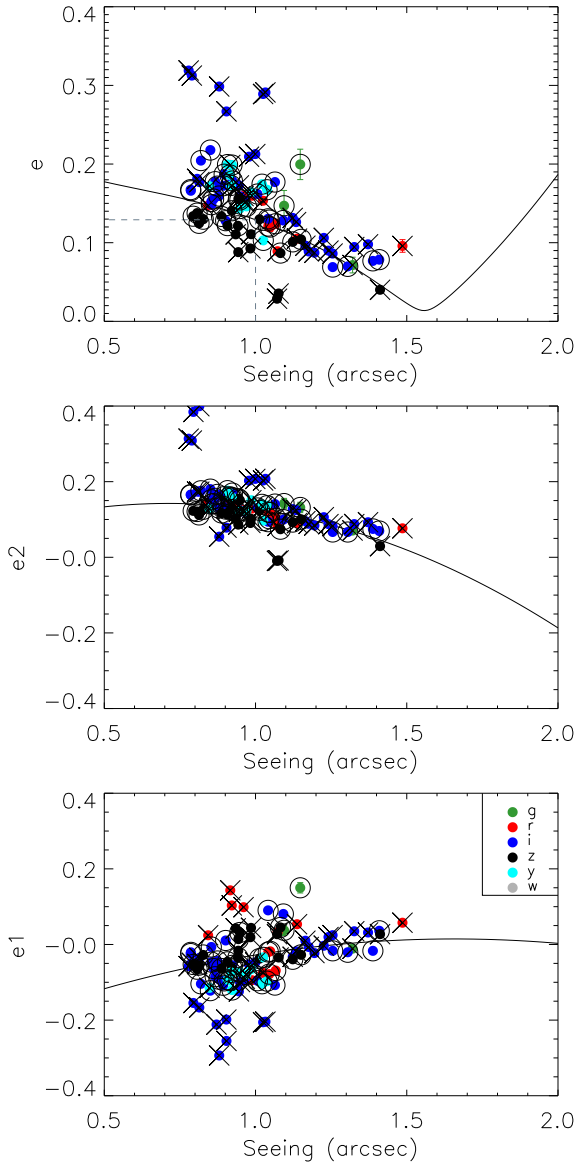


**Figure 12.** Ellipticity measurements and fits for LP 44−334. The top plot shows the total ellipticity, the middle plot the '×' polarization $e_2$ and the bottom plot the '+' polarization $e_2$. Points used in the second-order polynomial fits are outlined by a circle and those rejected for data quality reasons are crossed out. Note that due to the coordinate system of the postage stamps used, a positive $e_2$ is an elongation in the NW–SE direction and a positive $e_1$ is an elongation along the $x$ (i.e. R.A.) axis.

The value of $\nu$ here can either be 1 or 2, so for example, the final equation above is equivalent to equation (4). Parameters such as $X\nu\nu$_sm_OBJ are a shorthand for the data base parameters $X11$_sm_OBJ or $X22$_sm_OBJ, etc.

We extracted the detections for the sample of stars from Terziev et al. (2013). We then applied the correction procedure to each image to produce PSF anisotropy corrected shape measurements for each object. The results are shown in Fig. 15. Clearly, we are able to detect the closer (<1.5 arcsec) binaries but do not measure any significantly distorted images from the wider binaries. The reason for this is that the PS1 data base shape measurement calculations are based on the position of the primary star in the stacked PS1 images. Conversely in our image-based method, we used positions from SExtractor with no deblending, in reality intentionally blurring the image so the centroid position of the blended image is used as the central position for shape measurement calculations. Recall that this was to stop the centroid used for shape measurement changing if the secondary was resolved by SExtractor in a handful of images. This would result in an image centroid between the two components, thus producing higher image ellipticities than the case where the centroid is on the centre of the brighter binary component as the flux from the secondary will be more strongly suppressed by the weighting function. Note that all of the test sample binaries wider than 2.01 arcsec had their secondary component detected as an individual star in the PS1 data base. However, there is a blindspot for this method from the current data base between 1.5 arcsec and 2 arcsec where we would miss a substantial number of binaries.

### 5.1 Correction for centroiding errors

Our PS1 data base shape measurements rely on the positions of the objects in the stacked image data. For objects with little or no proper motion, this will produce accurate ellipticity measurements. However, if the object moves over the course of the PS1 survey then the ellipticity measurement will be artificially raised. This is because the image moments will be calculated relative to a position that will not represent the centroid of each individual detection. This implies that the error in the ellipticity should rise as $\Delta\mathrm{pos}^2$. There is however another factor, the weighting function that excludes flux far away from the centroid used in the calculation.

First, we must consider how the positional offset affects the two ellipticity polarizations,

$$\Delta\mathrm{pos}_1 = -\mu\Delta t\cos\left(\frac{\pi\mathrm{P.A.}}{90}\right)$$
$$\Delta\mathrm{pos}_2 = -\mu\Delta t\sin\left(\frac{\pi\mathrm{P.A.}}{90}\right). \quad (10)$$

We simulated the offset in ellipticity caused by positional offset by taking a Gaussian PSF and moving the centroid position about

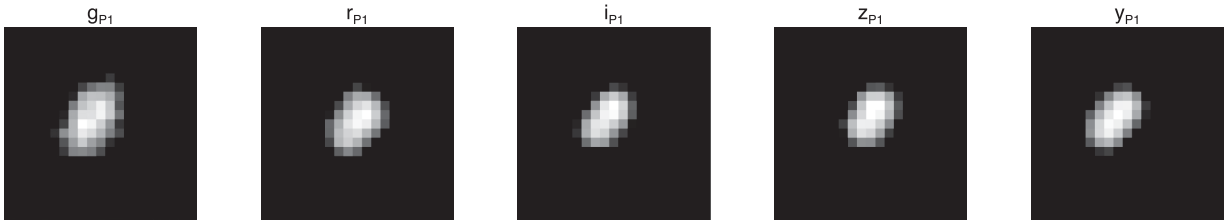


**Figure 13.** PS1 images of LP 44−334. All images are 5 arcsec across with north up and east left. The two components are separated by roughly 0.7 arcsec with the northwestern component marginally brighter.

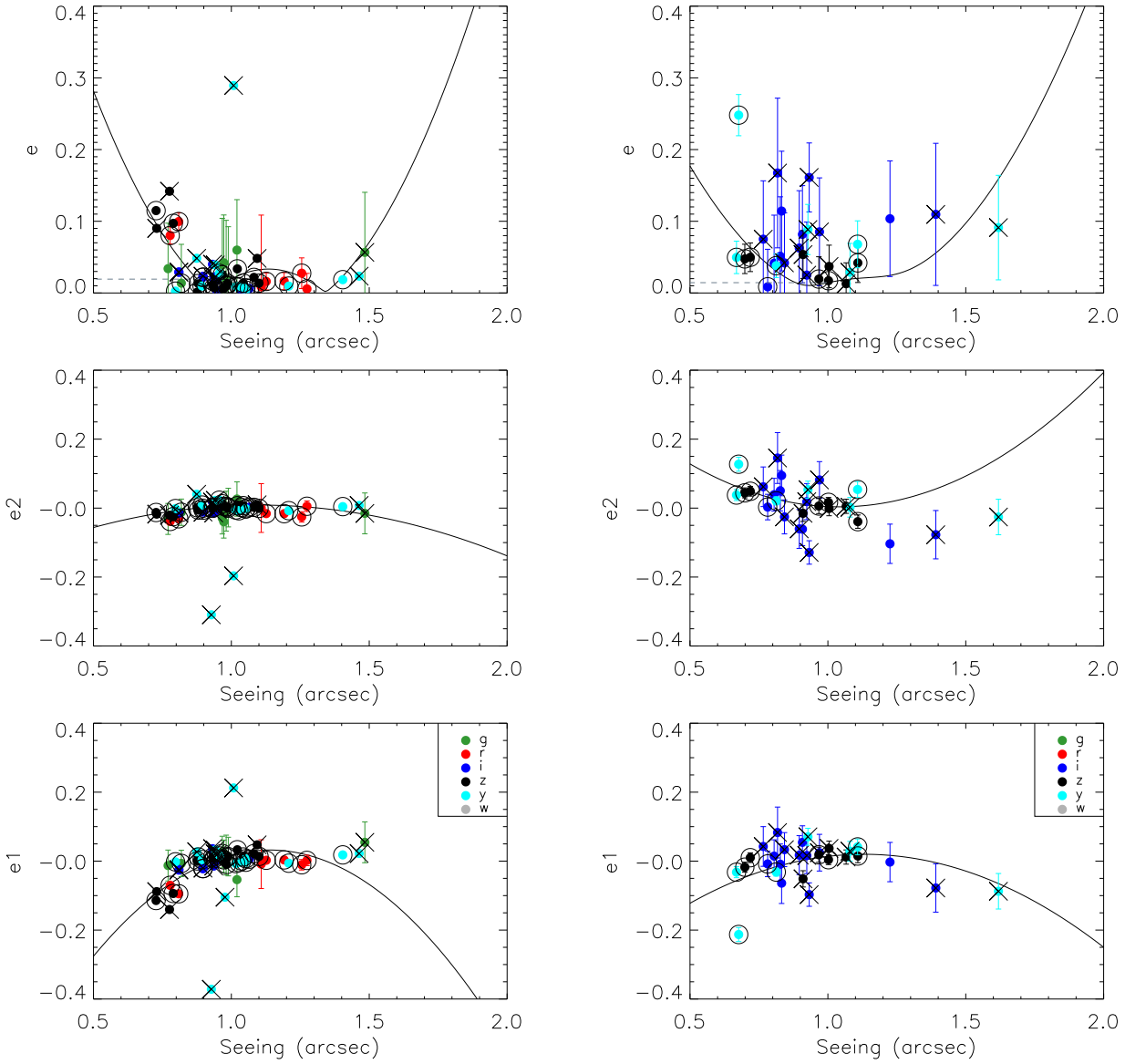


**Figure 14.** Ellipticity measurements and fits for the known binaries 2MASSI J0746425+200032 (left) and 2MASS J21522609+0937575 (right). Neither of these objects had a significant ellipticity at the reference seeing but they do show a clear trend at better seeing. The top plot shows the total ellipticity, the middle plot the '×' polarization $e_2$ and the bottom plot the '+' polarization $e_2$. Points used in the second-order polynomial fits are outlined by a circle and those rejected for data quality reasons are crossed out. Note that due to the coordinate system of the postage stamps used, a positive $e_2$ is an elongation in the NW–SE direction and a positive $e_1$ is an elongation along the $x$ (i.e. R.A.) axis.

which we measure the flux distribution. We used a series of different seeing FWHM values and found that the change in ellipticity was well modelled by

$$|\Delta e| = \frac{(\Delta\mathrm{pos}/\mathrm{FWHM})^2}{0.08 + (\Delta\mathrm{pos}/\mathrm{FWHM})^2}. \quad (11)$$

Thus,

$$\Delta e_1 = \mathrm{sgn}(\Delta\mathrm{pos}_1)\frac{(\Delta\mathrm{pos}_1/\mathrm{FWHM})^2}{0.08 + (\Delta\mathrm{pos}_1/\mathrm{FWHM})^2}$$

$$\Delta e_2 = \mathrm{sgn}(\Delta\mathrm{pos}_2)\frac{(\Delta\mathrm{pos}_2/\mathrm{FWHM})^2}{0.08 + (\Delta\mathrm{pos}_2/\mathrm{FWHM})^2}. \quad (12)$$

We note that these are approximations and are likely only useful for small offsets. Our work on the Terziev test sample (which typically has proper motions below 0.1 arcsec yr$^{-1}$) shows that binaries can be reliably detected for low proper motion objects without corrections. We would strongly caution that shape measurements for higher proper motion stars may be unreliable even after applying a correction factor.

## 6 CONCLUSIONS

We have applied shape measurement techniques to recover previously known binaries and discover three new binaries. We show that this method can reliably recover binaries wider than around 0.3 arcsec. The PS1 data base includes an implementation of stellar shape measurements that will hopefully become available in a future data release. These data will allow efficient screening of adaptive optics observations for close binaries. Future large surveys such as

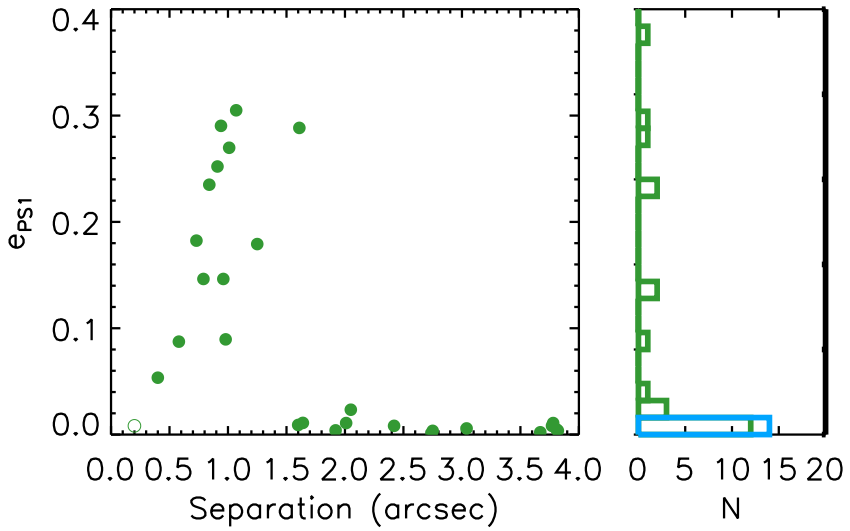


**Figure 15.** Left: the measured ellipticities at our reference seeing of 1 arcsec for binaries in the test sample of Terziev et al. (2013) produced using the image shape parameters from the PS1 data base alone. The open circle is an object with a very small separation which Terziev notes would not have affected the ellipticity measurement. Right: a histogram of these ellipticities for binaries (green) and single stars (blue). Note the one binary at a separation of 2 arcsec that has a low ellipticity. This has the smallest flux ratio in the sample at 0.04.

LSST would benefit from the availability of individual observation anisotropy parameters from all stellar objects. This would allow the study of large samples of partially resolved binaries to probe stellar multiplicity.

## ACKNOWLEDGEMENTS

The Pan-STARRS1 (PS1) surveys have been made possible through contributions of the Institute for Astronomy, the University of Hawaii, the Pan-STARRS Project Office, the Max-Planck Society and its participating institutes, the Max Planck Institute for Astronomy, Heidelberg and the Max Planck Institute for Extraterrestrial Physics, Garching, The Johns Hopkins University, Durham University, the University of Edinburgh, Queen's University Belfast, the Harvard–Smithsonian Center for Astrophysics, the Las Cumbres Observatory Global Telescope Network Incorporated, the National Central University of Taiwan, the Space Telescope Science Institute, the National Aeronautics and Space Administration under Grant No. NNX08AR22G issued through the Planetary Science Division of the NASA Science Mission Directorate, the National Science Foundation under Grant No. AST-1238877, the University of Maryland and Eotvos Lorand University (ELTE). Partial support for this work was provided by National Science Foundation grants AST-1313455 (EAM and WMJB) and NSF-AST-1518339 (MCL and WMJB). The authors would like to thank Adam Kraus, Emil Terziev, Nick Law, Thomas Dixon and Nick Kaiser for useful discussions.

## REFERENCES

Artigau É. et al., 2011, ApJ, 739, 48
Baranec C. et al., 2012, in Ellerbroek B. L., Marchetti E., Véran J.-P., Proc. SPIE Conf. Ser. Vol. 8447, Adaptive Optics Systems III. SPIE, Bellingham, p. 844704
Bertin E., Arnouts S., 1996, A & AS, 117, 393
Best W. M. J. et al., 2017, preprint (arXiv:1701.00490)
Bouy H., Brandner W., Martn E. L., Delfosse X., Allard F., Basri G., 2003, AJ, 126, 1526
Bouy H. et al., 2004, A&A, 423, 341
Burgasser A. J., McElwain M. W., 2006, AJ, 131, 1007
Burgasser A. J., Dhital S., West A. A., 2009, AJ, 138, 1563
Chabrier G., 2003, ApJ, 586, L133
Chambers K. C. et al., 2016, preprint (arXiv:1612.05560)
Close L. M., Siegler N., Freed M., Biller B., 2003, AJ, 587, 407
Cross N. J. G. et al., 2012, A&A, 548, A119
Diolaiti E., Bendinelli O., Bonaccini D., Close L., Currie D., Parmeggiani G., 2000, A&AS, 147, 335
Dupuy T. J., Liu M. C., 2012, ApJS, 201, 19
Fu H. et al., 2012, ApJ, 753, 134
Gelino C. R. et al., 2014, AJ, 148, 6
Hoekstra H., Franx M., Kuijken K., Squires G., 1998, ApJ, 504, 626
Hoekstra H., Wu Y., Udalski A., 2005, ApJ, 626, 1070
Howell S. B. et al., 2014, PASP, 126, 398
Kaiser N., Squires G., Broadhurst T., 1994, ApJ, 449, 39
Konopacky Q. M., Ghez A. M., Barman T. S., Rice E. L., Bailey J. I., White R. J., McLean I. S., Duchêne G., 2010, ApJ, 711, 1087
Kraus A. L., Ireland M. J., 2012, ApJ, 745, 5
Law N. M. et al., 2009, PASP, 121, 1395
Law N. M. et al., 2014, ApJ, 791, 35
Liu M. C., Leggett S. K., 2005, ApJ, 634, 616
Liu M. C., Dupuy T. J., Ireland M. J., 2008, ApJ, 689, 436
Mace G. N. et al., 2013, ApJS, 205, 6
McElwain M. W., Burgasser A. J., 2006, AJ, 132, 2074
Markwardt C. B., 2009, in Bohlender D. A., Durand D., Dowler P., eds. ASP Conf. Ser. Vol. 411, Astronomical Data Analysis Software and Systems XVIII. Astron. Soc. Pac., San Francisco, p. 251
Reid I. N., Gizis J. E., Kirkpatrick J. D., Koerner D. W., 2001, AJ, 121, 489
Reid I. N. et al., 2004, AJ, 128, 463
Reid I. N., Lewitus E., Allen P. R., Cruz K. L., Burgasser A. J., 2006, AJ, 132, 891
Reid I., Cruz K. L., Kirkpatrick J. D., Allen P. R., Mungall F., Liebert J., Lowrance P., Sweet A., 2008, AJ, 136, 1290
Sirko E., Paczynski B., 2003, ApJ, 592, 1217
Terziev E. et al., 2013, ApJS, 206, 18
Tonry J. L. et al., 2012, ApJ, 750, 99

Yelda S., Lu J. R., Ghez A. M., Clarkson W., Anderson J., Do T., Matthews K., 2010, ApJ, 725, 331

## SUPPORTING INFORMATION

Supplementary data are available at *MNRAS* online.

**Table 2.** A list of objects that did not have ellipticity at the reference seeing greater than 0.02 and more significant than $4\sigma$.

Please note: Oxford University Press is not responsible for the content or functionality of any supporting materials supplied by the authors. Any queries (other than missing material) should be directed to the corresponding author for the article.

This paper has been typeset from a TEX/LATEX file prepared by the author.